The Astrophysical Journal, 714:758–771, 2010 May 1 doi:10.1088/0004-637X/714/1/758

CAVITIES AND SHOCKS IN THE GALAXY GROUP HCG 62 AS REVEALED BY *CHANDRA*, *XMM-NEWTON*, AND GIANT METREWAVE RADIO TELESCOPE DATA

Myriam Gitti[1,2], Ewan O'Sullivan[1,3], Simona Giacintucci[1,4], Laurence P. David[1], Jan Vrtilek[1], Somak Raychaudhury[3], and Paul E. J. Nulsen[1]
[1] Harvard-Smithsonian Center for Astrophysics, 60 Garden Street, Cambridge, MA 02138, USA
[2] Astronomical Observatory of Bologna-INAF, via Ranzani 1, I-40127 Bologna, Italy
[3] University of Birmingham, Edgbaston, Birmingham B15 2TT, UK
[4] Institute of Radioastronomy-INAF, via Gobetti 101, I-40129 Bologna, Italy
Received 2009 December 15; accepted 2010 March 14; published 2010 April 14

ABSTRACT

We report on the results of an analysis of *Chandra*, *XMM-Newton*, and new Giant Metrewave Radio Telescope (GMRT) data of the X-ray bright compact group of galaxies HCG 62, which is one of the few groups known to possess clear, small X-ray cavities in the inner regions. This is part of an ongoing X-ray/low-frequency radio study of 18 groups, initially chosen for the availability of good-quality X-ray data and evidence for active galactic nucleus/hot gas interaction. At higher frequency (1.4 GHz), the HCG 62 cavity system shows minimal if any radio emission, but the new GMRT observations at 235 MHz and 610 MHz clearly detect extended low-frequency emission from radio lobes corresponding to the cavities. By means of the synergy of X-ray and low-frequency radio observations, we compare and discuss the morphology, luminosity, and pressure of the gas and of the radio source. We find that the radio source is radiatively inefficient, with a ratio of radio luminosity to mechanical cavity power of $\sim 10^{-4}$, and that the radio pressure of the lobes is about 1 order of magnitude lower than the X-ray pressure of the surrounding thermal gas. Thanks to the high spatial resolution of the *Chandra* surface brightness and temperature profiles, we also identify a shock front located at 36 kpc to the southwest of the group center, close to the southern radio lobe, with a Mach number ~ 1.5 and a total power which is about 1 order of magnitude higher than the cavity power. Such a shock may have heated the gas in the southern region, as indicated by the temperature map. The shock may also explain the arc-like region of enriched gas seen in the iron abundance map, as this may be produced by a non-Maxwellian electron distribution near its front.

Key words: galaxies: active – galaxies: clusters: general – galaxies: clusters: individual (HCG 62) – intergalactic medium – X-rays: galaxies: clusters

Online-only material: color figures

1. INTRODUCTION

Many possibilities have been proposed in the last decade to solve the so-called "cooling flow problem" in the hot atmospheres of galaxy clusters and groups, i.e., the lack of evidence for central gas cooling to very low temperatures at the rates predicted (see, e.g., the review by Peterson & Fabian 2006). Among these, feedback by the central active galactic nucleus (AGN) appears to be the most promising solution. Identifying radio galaxies (galaxies whose AGN produces the radio-emitting jets) as a primary source of feedback in clusters has been one of the major achievements of the current generation of X-ray observatories. Although gas does cool at least through part of the X-ray emitting temperature band (10^7–10^8 K) in galaxy clusters, *Chandra* and *XMM-Newton* have shown that there is not a significant amount of gas cooling below about one-third of its original temperature (e.g., Peterson et al. 2003; Kaastra et al. 2004). These observations also reveal highly disturbed structures in the cores of many clusters, including shocks, cavities, and sharp density discontinuities. At radio wavelengths, it is clear that AGN jets are the cause of many of these disturbances. The most typical configuration is for jets from the central dominant elliptical of a cluster to extend outwards and inflate lobes of radio-emitting plasma. These lobes push aside the X-ray emitting gas of the cluster atmosphere, thus leaving apparent cavities in the X-ray images (e.g., for a review, see McNamara & Nulsen 2007, and references therein).

There are already several in-depth analyses of individual rich clusters (e.g., Perseus: Fabian et al. 2006; Centaurus: Sanders et al. 2008; MS0735.6+7421: Gitti et al. 2007; A2052: Blanton et al. 2009) and studies of cluster samples (Bîrzan et al. 2004, 2008; Dunn et al. 2005; Dunn & Fabian 2006; Rafferty et al. 2006; Diehl et al. 2008). However, the differences between groups and clusters imply that the existing studies on feedback tell us little about how it operates in groups. Furthermore, due to the shallower group potential, the AGN outburst is expected to have a large impact on the intragroup medium. It is therefore essential to study individual groups and group samples in order to understand how feedback has influenced the thermal history of galaxies and the intragroup medium, and thus of most of the baryons in the universe. Such investigations have been undertaken only recently (e.g., Johnson et al. 2009; Sun 2009; Gastaldello et al. 2008, 2009; O'Sullivan et al. 2010; S. Giacintucci et al. 2010, in preparation).

The work presented here is part of an ongoing project aimed at combining X-ray and low-frequency radio observations of galaxy groups. In particular, we have selected a sample of 18 galaxy groups based on the presence of signs of interaction between the hot gas and the central AGN. For these groups, which all have good-quality X-ray data in the archives of *Chandra* and/or *XMM-Newton*, we have obtained new radio data at the Giant Metrewave Radio Telescope (GMRT) at 235 MHz, 327 MHz, and 610 MHz (Giacintucci et al. 2008, 2009; Raychaudhury et al. 2009; S. Giacintucci et al. 2010, in preparation).

HCG 62 ($z = 0.0137$) is the X-ray brightest of the Hickson compact groups and has been extensively studied with *ROSAT*, *ASCA*, *Chandra*, *XMM-Newton*, and *Suzaku* (Ponman & Bertram 1993; Finoguenov & Ponman 1999; Buote 2000; Morita et al. 2006; Gu et al. 2007; Tokoi et al. 2008; Sanders et al. 2010). The central region of this group is dominated by four early-type galaxies, two of which are likely interacting as indicated by optical studies (Valluri & Anupama 1996; Spavone et al. 2006). This was the first galaxy group with a clear detection of inner cavities (Vrtilek et al. 2002). The existing 1.4 GHz Very Large Array observations mainly show the emission from the compact radio source and indicate only some hints of extended radio emission toward the southern cavity (Vrtilek et al. 2002). Owing to the poor radio images then available, the HCG 62 cavity system was classified as a "radio ghost" in the sample of Bîrzan et al. (2004).

We present here new low-frequency GMRT radio observations of HCG 62 that, together with the existing X-ray *Chandra* and *XMM-Newton* observations, allow us to study the X-ray/radio interaction and investigate the AGN feedback in this group. This paper is organized as follows. In Section 2 we describe the data sets used for our investigation and the data reduction process, in Section 3 we show the X-ray and radio morphologies of the group inner region, and in Section 4 we present the X-ray properties derived from the spectral analysis. In Section 5.1, we investigate the interaction of the radio plasma with the hot gas in terms of energetics (Section 5.1.1) and pressure balance (Section 5.1.2). In Section 5.2, we analyze the surface brightness discontinuities, finding evidence for the detection of weak shocks. Finally, in Section 5.3, we present the two-dimensional distribution of temperature (Section 5.3.1) and iron abundance (Section 5.3.2). The summary of our main results is given in Section 6.

With $H_0 = 70\,\mathrm{km\,s^{-1}\,Mpc^{-1}}$ and $\Omega_M = 1 - \Omega_\Lambda = 0.3$, the luminosity distance to HCG 62 is 59 Mpc and 1 arcsec corresponds to 0.28 kpc in the rest frame of the group. The radio spectral index α is defined as $S_\nu \propto \nu^{-\alpha}$, where S_ν is the flux density at frequency ν.

2. OBSERVATIONS AND DATA REDUCTION

2.1. Chandra

HCG 62 was observed with *Chandra* for ∼48.5 ks on 2000 January 25 (ObsID 921) with ACIS-S in imaging mode operating at the focal plane temperature of −110°C. The data were reprocessed with CIAO 4.1 using CALDB 4.1.0 and corrected for known time-dependent gain problems following techniques similar to those described in the *Chandra* analysis threads.[5] No charge transfer inefficiency (CTI) correction is available for data taken at −110°C. Screening of the event files was applied to filter out strong background flares. Blank-sky background files, filtered in the same manner as in the HCG 62 image and normalized to the count rate of the source image in the 10.0–12.0 keV band, were used for background subtraction. The final exposure time is 46.5 ks. We only use data from the S3 CCD since it covers the central part of the group emission where the cavity system and the radio source are located. We identified and removed the point sources on S3 using the CIAO task `WAVDETECT`, with the detection threshold set to the default value of 10^{-6}.

[5] http://cxc.harvard.edu/ciao/threads/index.html

Updated gain correction at −110°C only become available with CIAO 4.0 CALDB version, so previous work has been limited by calibration uncertainties. In particular, spectra were extracted using the `SPECEXTRACT` task and, as recommended for −110°C data,[6] new RMF files were computed using the task `MKACISRMF` with the latest gain file, `acisD2000-01-29p2_respN0005.fits`.

2.2. XMM-Newton

HCG 62 was observed by *XMM-Newton* in 2007 June during revolutions 1382 (ObsID 0504780501, hereafter 501) and 1383 (ObsID 0504780601, hereafter 601) for nominal exposure times of 122.5 ks and 32 ks, respectively. In this paper, only data from the European Photon Imaging Camera (EPIC) are presented. The MOS detectors were operated in Full Frame Mode and the PN detector in Extended Full Frame Mode, both with the MEDIUM filter. We used the SASv8.0.0 processing tasks `emchain` and `epchain` to generate calibrated event files from raw data. Throughout this analysis single and double pixel events for the PN data (PATTERN <=4) were selected, while for the MOS data sets the PATTERNs 0–12 were used. The removal of bright pixels and hot columns was done by applying the expression (FLAG==0). To reject soft proton flares, we generated a light curve in the 10.0–12.0 keV band where the emission is dominated by the particle-induced background, and excluded all the intervals of exposure time having a count rate higher than a certain threshold value (the chosen threshold values are 0.20 (0.18) cps for MOS and 0.35 (0.32) cps for PN in obs. 501 (601)). The total remaining exposure times after cleaning are 112.0 ks for MOS1, 97.6 ks for MOS2, and 60.2 ks for PN. Starting from the output of the SAS detection source task, we made a visual selection on a wide energy band MOS and PN image of point sources in the field of view. Events from these regions were excluded directly from each event list. The source and background events were corrected for vignetting using the weighted method described in Arnaud et al. (2001), the weight coefficients being tabulated in the event list with the SAS task `evigweight`. This allows us to use the on-axis response matrices and effective areas, computed in the central 30″ with the tasks `rmfgen` and `arfgen`.

2.2.1. Background Treatment

The background estimates are derived using blank-sky observations consisting of a superposition of pointed observations that have been processed with SAS version 7.1.0 (Carter & Read 2007). In particular, for each camera, we obtained a blank-sky template tailored to the characteristics of HCG 62 specific observation by submitting an *XMM-Newton* EPIC Background Blank Sky Products Request Form[7] with the request[8] of a Galactic column in the range 2 to 5 $\times 10^{20}\,\mathrm{cm^{-2}}$.

The blank-sky background events were then selected using the same selection criteria (such as PATTERN, FLAG, etc.), intensity filter (for flare rejection), and point-source removal used for the observation events. This yields final exposure times for the blank fields of 1.0 Ms for MOS1, 1.6 Ms for MOS2, and 99.3 ks for PN. Since the cosmic-ray-induced background

[6] http://cxc.harvard.edu/ciao/why/110.html

[7] http://www.star.le.ac.uk/~jac48/BG/UserRequest/blankskyform.html

[8] The selection criteria adopted are as follows. Filter: medium; model: full-frame (extended full-frame for PN); type: ghosted; Galactic column: 2.0–5.0 × $10^{20}\,\mathrm{cm^{-2}}$; Equatorial coordinates: (193.274, −9.2036) degrees; radius = 180 degrees.

might change slightly with time, we computed the ratio of the total count rates in the high-energy band (10.0–12.0 keV). The obtained normalization factors (1.258 (1.203), 1.316 (1.246), 1.353 (1.175) for MOS1, MOS2, and PN, respectively, in obs. 501 (601)) were then used to renormalize the blank field data. The blank-sky background files were finally recast in order to have the same sky coordinates as HCG 62.

The usual approach to perform the background subtraction is described in full detail in Arnaud et al. (2002). This procedure consists of two steps. In the first step, for each spectrum extracted from the observation event list an equivalent spectrum is extracted from the corresponding blank-field file and then subtracted from it. This allows us to remove the particle background. However, if the background in the observation region is different from the average background in blank field data, this step could leave a residual background component. The residual background component is estimated by using blank-field-subtracted data in a region supposedly free of source emission (in particular, we considered an annulus lying between 13 and 14 arcmin) and then subtracted in a second step from each MOS and PN spectrum. We note that while some group emission might still fall in the annulus chosen to estimate the residual background component, our spectral analysis is not affected as the central region we are interested in is very bright and source dominated.

2.3. GMRT

HCG 62 was observed by the GMRT in 2008 February at frequencies of 610 MHz and 235 MHz (project 13SGa01) for a total of 125 and 250 minutes, respectively. The data were acquired in spectral line mode with 128 channels/band and a bandwidth of 16 MHz at 610 MHz and 8 MHz at 235 MHz. Data reduction was done using the NRAO Astronomical Image Processing System (AIPS) package. Accurate editing of the UV data was applied to identify and remove bad data. After bandpass calibration, the central channels were averaged to six channels of ∼2 MHz at 610 MHz and ∼1 MHz at 235 MHz. After further careful editing in the averaged data sets, images were produced using the standard procedure (calibration, Fourier transform, clean, and restore) and the wide-field imaging technique. Phase-only self-calibration was applied to remove residual phase variations. The rms noise level (1σ) in the final images is 50 μJy beam^{-1} at 610 MHz and 170 μJy beam^{-1} at 235 MHz. Following Chandra et al. (2004), we estimated that the amplitude calibration error at 610 MHz is ∼5%, while a calibration error of 8% was assumed at 235 MHz. The calibration uncertainties were included in the flux density and spectral index errors determined in Section 3.2. The GMRT observations of HCG 62 will be presented and discussed in more detail in S. Giacintucci et al. (2010, in preparation).

3. THE DISTURBED INNER REGION OF HCG 62

3.1. X-ray Morphology

The raw 0.5–2.0 keV ACIS-S image in Figure 1 (top left panel) shows that the hot gas in the central region of HCG 62 is not smoothly distributed but is instead perturbed with cavities and edges. In particular, as best revealed by the unsharp masked image shown in Figure 1 (top right panel), we confirm the presence of two clear cavities, first discovered by Vrtilek et al. (2002), and we also notice the presence of surface brightness discontinuities or "fronts" which suggest the presence of large-scale gas motions or shocks in the group halo. In particular, by means of the surface brightness profiles presented in Section 5.2, we identify a front at 36 kpc (∼2′) from the center toward the southwest (SW) at a distance of about 10 kpc (∼35″) from the southern radio lobe, and one at 20 kpc (∼70″) from the center toward the northeast (NE) close to the N cavity. These features are significant at the 5σ and 15σ levels, respectively. In the images, there is also a hint of an edge about the same distance SW of the group center as the front to the NE. The spectral analysis presented below indicates that the outer SW edge is a shock front (Section 5.2). As already estimated by previous studies (Bîrzan et al. 2004; Rafferty et al. 2006; Morita et al. 2006) the two cavities have similar sizes, with diameters of ∼10 kpc, and are located at a projected distance of ∼8.5 kpc from the group center. We extracted the surface brightness profiles along and orthogonal to the cavities, and at the radius of ∼8.5 kpc we estimate a brightness decrement of ∼30% along the cavities relative to the orthogonal direction.

Because of the poorer *XMM-Newton* spatial resolution, the cavities are not evident in the raw 0.5–2.0 keV image shown in Figure 1 (bottom left panel). However, they do appear clearly in the unsharp masked image (Figure 1, bottom right panel) at positions coincident with those determined by the *Chandra* data.

3.2. Radio Properties

The existing higher frequency (1.4 GHz) observations of HCG 62 show the central compact radio source with some hint of emission extending toward the southern cavity (Vrtilek et al. 2002). With the new GMRT observations at 235 MHz and 610 MHz, we detect clearly extended emission emanating from the core in the typical form of a bipolar flow. The two radio lobes point toward the N and S directions, filling the cavities. The overlay of the 610 MHz radio contours on the unsharp masked *Chandra* image is shown in Figure 2 (left), whereas the overlay of the 235 MHz radio contours on the smoothed *Chandra* image is shown in Figure 2 (right). It is evident that far more extensive structures become visible at lower frequencies: the radio emission at 235 MHz is more extended with two faint regions located outside the cavities and apparently bent toward the east (E). In particular, we identify inner lobes clearly filling the well-defined X-ray cavities (best visible in the left panel of Figure 2), and outer lobes having no associated X-ray cavities (best visible in the right panel of Figure 2). The connection of the radio source with the X-ray features will be discussed in Section 5.

At 610 MHz, the source has a total flux density of 13.5 ± 0.7 mJy. At 235 MHz, the total flux density is 42.4 ± 3.4 mJy. Neglecting the *K-correction* term (for $0.3 < \alpha < 1.7$, the *K-correction* is < 1%; Petrosian & Dickey 1973), the monochromatic radio power at each frequency is calculated as

$$P_\nu = 4\pi\, D_{\rm L}^2\, S_\nu, \qquad (1)$$

where $D_{\rm L}$ is the luminosity distance, which gives $P_{610\,\rm MHz} = (5.7 \pm 0.3) \times 10^{21}$ W Hz^{-1} and $P_{235\,\rm MHz} = (1.8 \pm 0.1) \times 10^{22}$ W Hz^{-1}. This radio source is thus classified as a weak FR-I, and its spectral index $\alpha_{235\,\rm MHz}^{610\,\rm MHz} = 1.2 \pm 0.1$ is steep compared to that of typical radio galaxies.

Since the outer radio lobes are only detected at one frequency in our GMRT observations, we are unable to perform a detailed radio spectral analysis. New, deeper GMRT observations at 235, 327, and 610 MHz, scheduled during Cycle 17, will allow us to study with unprecedented detail the spectral properties of the

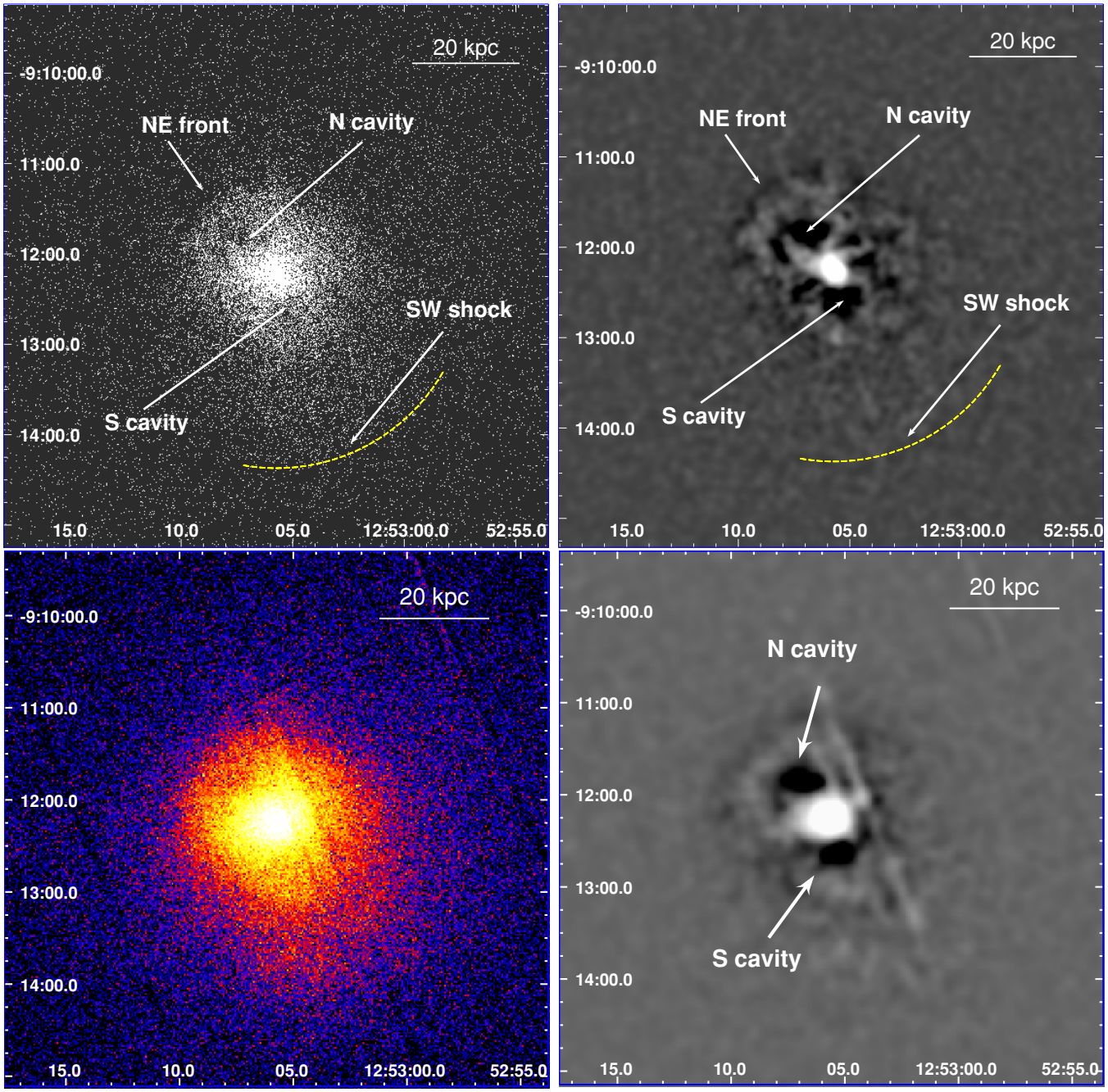

Figure 1. Top: raw (left) and unsharp masked (right) 0.5–2.0 keV ACIS-S image of the central region of HCG 62. Bottom: raw (left) and unsharp masked (right) 0.5–2.0 keV MOS1+MOS2+PN mosaic image of the central region of HCG 62. The unsharp masked images are produced by subtracting a large-scale (20 pixels) smoothed image from a small-scale (5 pixels) smoothed image. The arrows indicate the features discussed in the text (see Section 3.1). In particular, the dashed arc in the top panels indicates the position of the SW shock, which is non-visible clearly in the images. In all panels, the box is $6' \times 6'$ (101 kpc by 101 kpc). North is up and east is left.

(A color version of this figure is available in the online journal.)

source. Based on the analysis of the integrated radio spectrum and spectral index distribution, an estimate of the radiative ages of the electron population can be obtained (e.g., Giacintucci et al. 2007, 2008, and references therein) for both pairs of radio lobes. This will help to shed light on the relationship of the outer lobes to the inner ones.

4. GLOBAL X-RAY PROPERTIES

Throughout the analysis, a single spectrum for each instrument and each data set was extracted for each region of interest. The relative normalizations of the MOS and PN spectra were left free when fitted simultaneously. Spectral fitting was performed in XSPEC version 12.3.1. Abundances were measured relative to the abundance ratios of Anders & Grevesse (1989). A galactic hydrogen column of $3.31 \times 10^{20}\,\mathrm{cm}^{-2}$ (Dickey & Lockman 1990) and a redshift of 0.0137 was assumed and, unless otherwise stated, the reported errors are at the 90% confidence level. Spectra were grouped to 25 counts per bin and the energy range 0.7–3.0 keV was adopted.

We first tested in detail the consistency between *Chandra* and the three *XMM-Newton* cameras by extracting a global

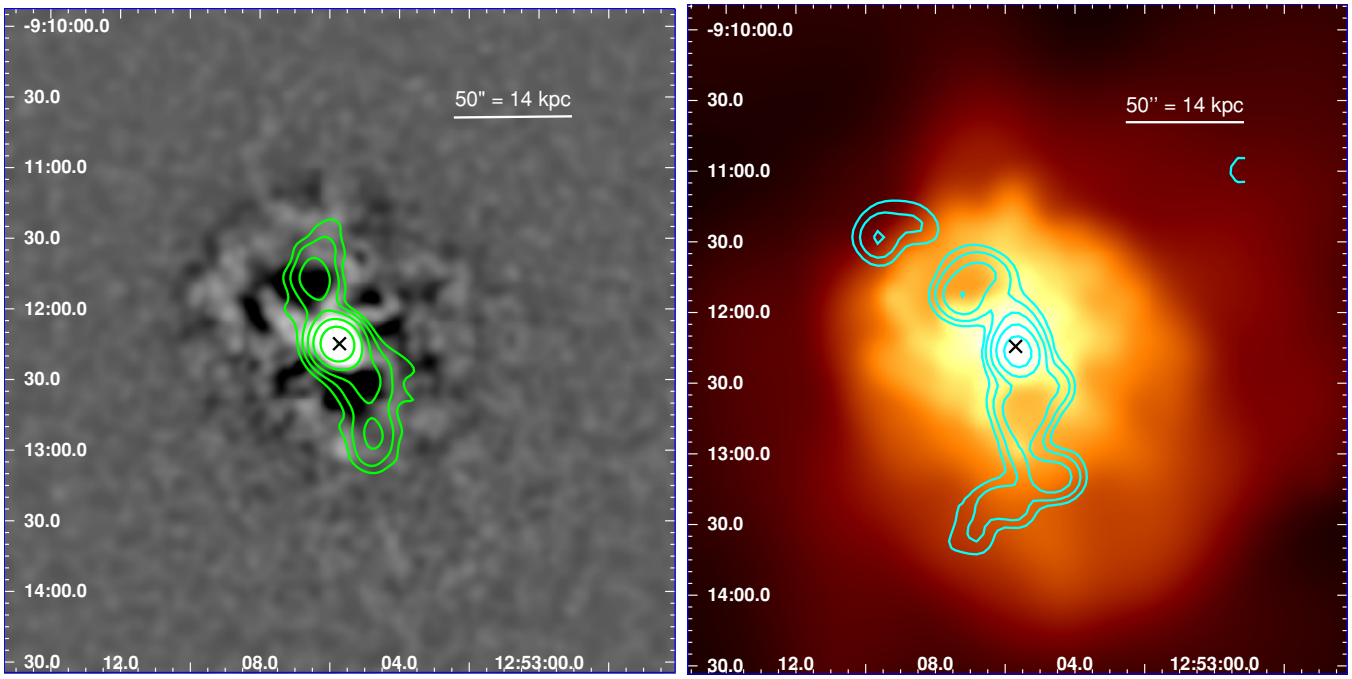

Figure 2. Left: GMRT 610 MHz contours overlaid on the unsharp masked 0.5–2.0 keV *Chandra* image (same as in the top right panel of Figure 1). The beam size is $14'' \times 14''$ and the lowest contour is shown at $3\sigma = 0.15$ mJy beam^{-1}. Right: GMRT 235 MHz contours overlaid on the smoothed 0.5–2.0 keV *Chandra* image. The beam size is $14\farcs4 \times 13''$ and the rms noise is 170 μJy beam^{-1}. The contours are spaced by a factor of 2 starting from the lowest level of 0.45 mJy beam^{-1}. In both panels, the cross indicates the position of the radio core. North is up and east is left.

(A color version of this figure is available in the online journal.)

spectrum from all events lying in the annulus 1–3 arcmin from the group emission peak and fitting these spectra separately with an absorbed `apec` model. We find good agreement between the three *XMM-Newton* cameras ($kT = 1.25^{+0.02}_{-0.02}$ keV for MOS1, $1.21^{+0.02}_{-0.02}$ keV for MOS2, $1.23^{+0.01}_{-0.01}$ keV for PN, with a value of $1.23^{+0.01}_{-0.01}$ for the combined fit), whereas there is a discrepancy of about 0.1 keV with the *Chandra* measurement ($kT = 1.32^{+0.01}_{-0.01}$ keV). However, this is consistent with the systematic cross-calibration uncertainties (David 2009). Due to the systematic offset, we analyzed *Chandra* and *XMM-Newton* data separately. In particular, we present here the results obtained by the analysis of *XMM-Newton* spectra only because they comprise most of the counts.

4.1. Azimuthally Averaged Projected Temperature and Metallicity Profiles

We produced projected radial temperature and metallicity profiles by extracting spectra in six circular annuli centered on the peak of the X-ray emission. The annular regions are described in Table 1. The data from the three *XMM-Newton* cameras were fitted simultaneously to an absorbed `vapec` thermal plasma model, where O, Si, S, and Fe are treated as free parameters with the Ni abundance linked to the Fe abundance and the Mg and Ne abundances linked to the O abundance. The best-fitting parameter values and 90% confidence levels derived from the fits to the 360° annular spectra are summarized in Table 1.

The azimuthally averaged projected temperature profile (Figure 3, left) shows a positive temperature gradient at small radii, with temperatures increasing up to ∼1.5 keV at a radius of ∼50 kpc. This behavior is similar to that observed in other groups (e.g., Gastaldello et al. 2007; Finoguenov et al. 2007; Rasmussen & Ponman 2007; Sun et al. 2009), although we do not observe the typical decline in temperature at larger radii. Previous *ROSAT* observations of HCG 62 indicate a temperature decline beyond ∼120 kpc (Ponman & Bertram 1993), so our result is consistent with the earlier literature.

The azimuthally averaged projected abundance profiles (Figure 3, right) do not show strong gradients, but are instead relatively flat around values of ∼0.5 solar for both Si and S, and ∼0.3 solar for Fe. We were able to constrain O only in the central region, with a value of ∼0.4 solar.

Table 1
XMM-Newton Projected Spectral Analysis

No.	kT (keV)	Mg, Ne, O (solar)	Si (solar)	S (solar)	Ni, Fe (solar)	χ^2/dof
1	$0.80^{+0.01}_{-0.01}$	$0.42^{+0.06}_{-0.05}$	$0.40^{+0.04}_{-0.04}$	$0.71^{+0.10}_{-0.09}$	$0.35^{+0.02}_{-0.02}$	1430/786
2	$1.06^{+0.01}_{-0.01}$	$0.08^{+0.07}_{-0.07}$	$0.28^{+0.04}_{-0.04}$	$0.48^{+0.09}_{-0.09}$	$0.25^{+0.01}_{-0.01}$	820/653
3	$1.30^{+0.01}_{-0.01}$	$0.00^{+0.06}_{-0.00}$	$0.51^{+0.07}_{-0.06}$	$0.52^{+0.13}_{-0.12}$	$0.39^{+0.03}_{-0.02}$	935/638
4	$1.40^{+0.06}_{-0.05}$	$0.14^{+0.20}_{-0.06}$	$0.40^{+0.10}_{-0.09}$	$0.60^{+0.18}_{-0.16}$	$0.29^{+0.05}_{-0.04}$	1000/578
5	$1.47^{+0.06}_{-0.04}$	$0.00^{+0.14}_{-0.00}$	$0.48^{+0.12}_{-0.11}$	$0.52^{+0.20}_{-0.20}$	$0.29^{+0.05}_{-0.04}$	1258/600
6	$1.48^{+0.06}_{-0.06}$	$0.00^{+0.02}_{-0.00}$	$0.57^{+0.09}_{-0.09}$	$0.55^{+0.17}_{-0.17}$	$0.22^{+0.03}_{-0.03}$	10273/1178

Notes. Results of the *XMM-Newton* spectral fitting in concentric 360° annular regions in the 0.7–3.0 keV energy range using the absorbed `vapec` thermal plasma model and fixing the absorbing column density to the Galactic value ($N_{\rm H} = 3.31 \times 10^{20}$ cm^{-2}). The temperature (in keV) and abundances (in fraction of the solar value; Anders & Grevesse 1989) are left as free parameters. Error bars are at the 90% confidence levels on a single parameter of interest. The first column indicates the number region. The delimiting radii are: reg.1: 0–15 kpc (0″–55″); reg.2: 15–28 kpc (55″–100″); reg.3: 28–42 kpc (100″–150″); reg.4: 42–56 kpc (150″–200″); reg.5: 56–70 kpc (200″–250″); reg.6: 70–126 kpc (250″–450″).

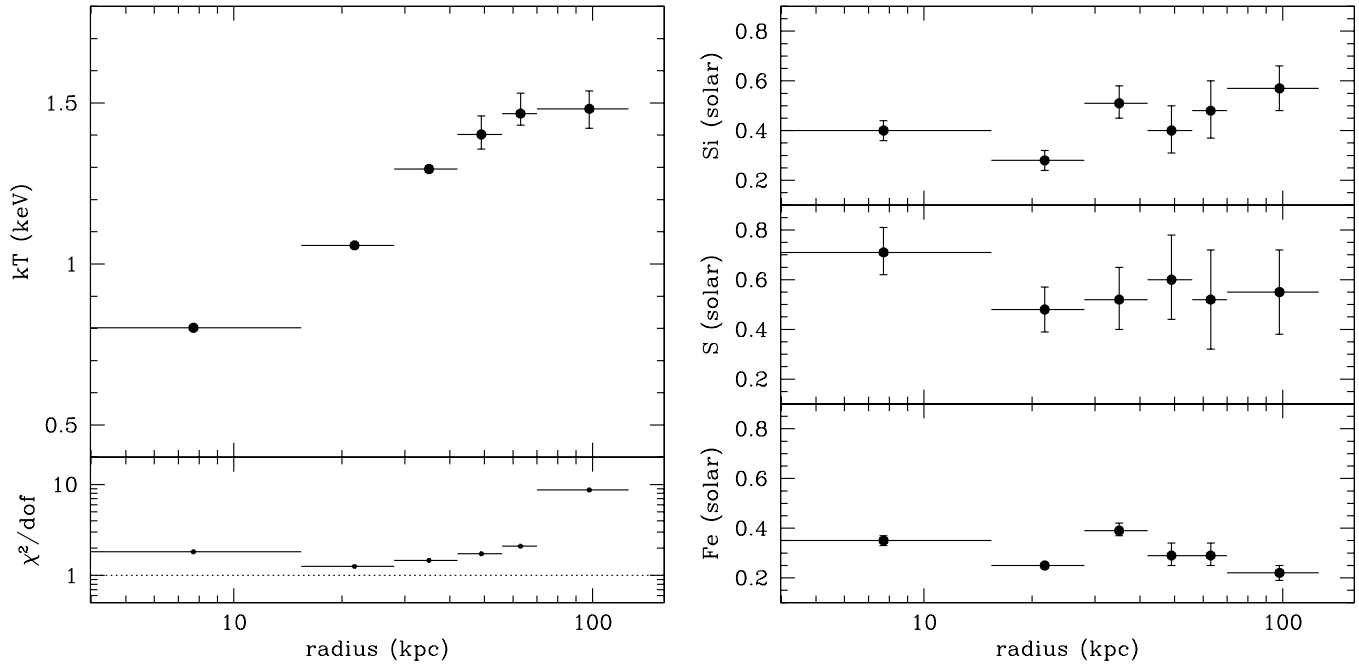

Figure 3. Left: azimuthally averaged projected temperature profile measured with *XMM-Newton* and reduced $\chi^2_\nu = \chi^2/\mathrm{dof}$ of the fit. Right: azimuthally averaged projected abundance profiles of Si, S, and Fe measured with *XMM-Newton*.

4.2. Deprojection Analysis

To correct for the effect of projection along the line of sight, we also performed a deprojection analysis on the same annular spectra used in Section 4.1 by adopting the XSPEC `projct` model. Under the assumption of ellipsoidal (in our specific case, spherical) shells of emission, this model calculates the geometric weighting factor, according to which the emission is redistributed amongst the projected annuli. As expected, the deprojected central temperature is lower than the projected one, since in the projected fits the spectrum of the central annulus is contaminated by hotter emission along the line of sight. We also note that the low value that we measure probably represents the very coolest gas in the core, owing to emission weighting in the large bin adopted to account for the *XMM-Newton* point-spread function. Due to the limited photon statistics relative to the high number of parameters in the `projct` model we could only poorly constrain the deprojected abundance profiles, which therefore are not shown.

We also estimate various quantities derived from the deprojected spectral fits. The electron density n_e is obtained from the Emission Integral $\mathrm{EI} = \int n_e n_p dV$ given by the `vapec` normalization: $10^{-14}\mathrm{EI}/(4\pi[D_A(1+z)]^2)$. We assume $n_p = 0.82 n_e$ in the ionized intra-cluster plasma. By starting from the deprojected density and temperature values, we can then calculate the gas pressure as $p = nkT$, where we assume $n = 2n_e$, and the gas entropy from the commonly adopted definition $S = kT\, n_e^{-2/3}$. The results are reported in Table 2 and the corresponding deprojected temperature, density, pressure, and entropy profiles are shown in Figure 4.

Table 2
XMM-Newton Deprojected Spectral Analysis

No.	kT (keV)	Ni, Fe (solar)	$n_e \times 10^{-3}$ (cm^{-3})	$P \times 10^{-12}$ ($\mathrm{erg\,cm}^{-3}$)	S ($\mathrm{keV\,cm}^2$)
1	$0.36^{+0.01}_{-0.01}$	...	$26.78^{+3.54}_{-3.99}$	$30.89^{+4.09}_{-4.61}$	$4.02^{+0.36}_{-0.40}$
2	$1.00^{+0.01}_{-0.01}$	$0.41^{+0.03}_{-0.02}$	$3.57^{+1.09}_{-0.62}$	$11.43^{+3.48}_{-2.00}$	$42.83^{+8.71}_{-4.99}$
3	$1.28^{+0.02}_{-0.02}$	$0.52^{+0.06}_{-0.05}$	$2.00^{+0.36}_{-0.43}$	$8.19^{+1.47}_{-1.76}$	$80.72^{+9.69}_{-11.59}$
4	$1.33^{+0.11}_{-0.04}$	$0.32^{+0.07}_{-0.04}$	$1.14^{+0.38}_{-0.43}$	$4.88^{+1.66}_{-1.82}$	$121.53^{+28.52}_{-30.31}$
5	$1.55^{+0.10}_{-0.12}$	$0.45^{+0.13}_{-0.12}$	$0.89^{+0.22}_{-0.30}$	$4.43^{+1.14}_{-1.50}$	$167.32^{+29.75}_{-39.03}$
6	$1.47^{+0.06}_{-0.06}$	$0.21^{+0.04}_{-0.03}$	$0.59^{+0.09}_{-0.12}$	$2.79^{+0.43}_{-0.59}$	$208.34^{+22.15}_{-29.87}$

Notes. Results of the *XMM-Newton* deprojection analysis in concentric 360° annular regions in the 0.7–3.0 keV energy range using the XSPEC `projct` × `wabs`×`mekal` model and fixing the absorbing column density to the Galactic value ($N_H = 3.31 \times 10^{20}\,\mathrm{cm}^{-2}$). The fit gives $\chi^2/\mathrm{dof} = 19848/4463$. The first column indicates the number region. The delimiting radii are the same as in Table 1.

4.3. Azimuthal Variations in Projected Temperature and Metallicity Profiles

The interaction of the radio source with the thermal gas can produce significant effects on the X-ray properties of the group halo that are thus expected to show azimuthal variations. To investigate this, we performed a spectral analysis in annular sectors each having angular aperture of 45°. Starting from the W direction with position angle (P.A.) = 0° and counting counterclockwise, the sectors are labeled as WN (westnorth), NW (northwest), NE (northeast), EN (eastnorth), ES (eastsouth), SE (southeast), SW (southwest), and WS (westsouth). Each sector was divided in the same six annular regions used in Section 4.1, obtaining the regions shown in Figure 5 (left panel). We produced projected radial temperature and metallicity profiles by extracting spectra in these regions. In particular, we compared the radial properties along and orthogonal to the radio lobes and cavity system. The northern and southern cavities fall entirely within the first annulus in the NE and SW sectors, respectively. The profiles derived along the different sectors are shown in Figure 5 (top right), while the temperature and metallicity wedge maps are shown in Figure 5 (bottom left and right, respectively). The gas properties do not appear to show variations obviously associated with the cavities and radio lobes. This indicates that the spectral analysis in large sectors is probably not the most sensitive way to study the two-dimensional distribution of

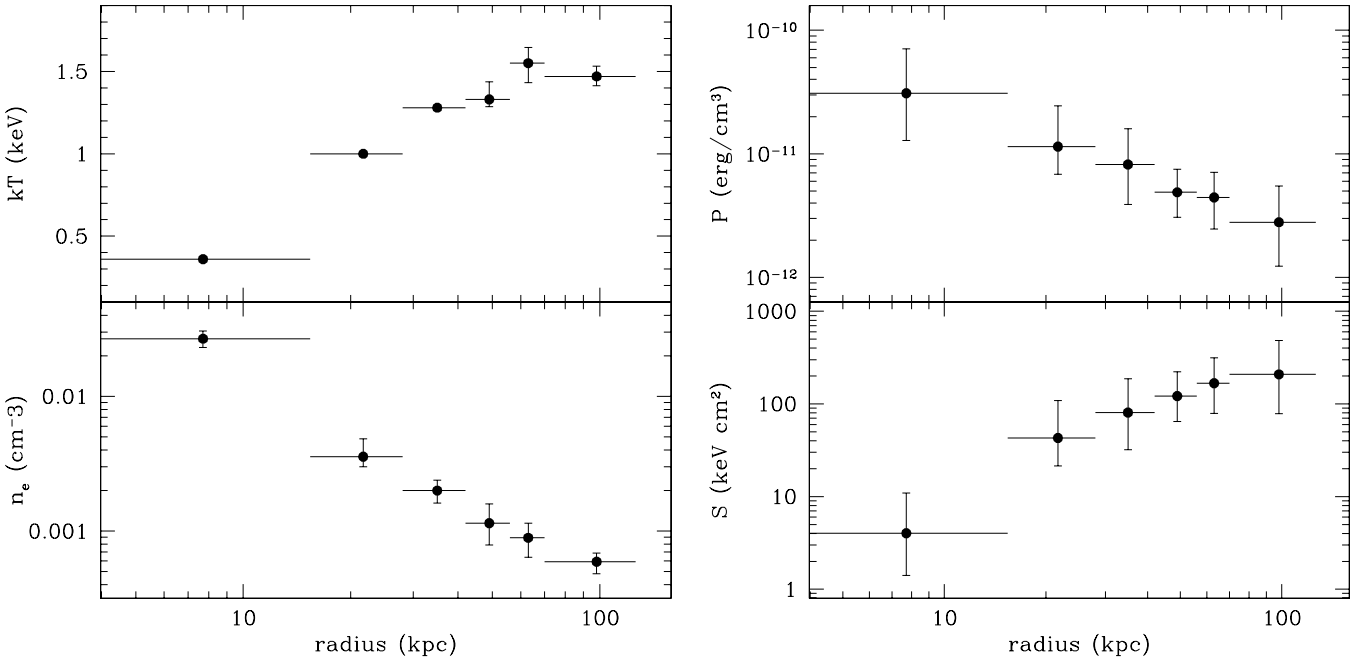

Figure 4. Left: azimuthally averaged deprojected profiles of temperature (top) and density (bottom) measured with *XMM-Newton*. Right: azimuthally averaged deprojected profiles of pressure (top) and entropy (bottom) measured with *XMM-Newton*.

temperature and metallicity in such a disturbed system as HCG 62. Higher-resolution spectral maps are presented and discussed in Section 5.3.

5. DISCUSSION

5.1. Interaction of the Radio Plasma with the Hot Gas

5.1.1. Energetics

We wish to compare the cavity power (which is a measure of the energy injected into the hot gas by the AGN outburst) with the gas luminosity inside the cooling radius (which represents the energy lost by the hot gas due to X-ray radiation). The total power of the two cavities can be estimated directly from the X-ray measurement of the pV work done by the jets in inflating the cavities, and from measurement of the cavity age (e.g., McNamara & Nulsen 2007). By measuring the cavity enthalpy as $H = 4pV$ (for a relativistic plasma) and the cavity age as the sound crossing time $t_s = R/c_s = R/\sqrt{\gamma kT/\mu m_{\rm H}}$, where R is the projected distance from the center of the cavity to the group center, $\gamma = 5/3$, and $\mu = 0.62$, we estimate that the total cavity power is $P_{\rm cav} = 3.8 \times 10^{42}\,{\rm erg\,s^{-1}}$, which is in agreement with the results of Bîrzan et al. (2004) and Rafferty et al. (2006). In particular, in deriving the sound speed c_s, we adopt the temperature values estimated in the first NE and SW sectoral annuli, respectively (see Section 4.3). The results are reported in Table 3. Given the uncertainties in estimating the cavity age, for comparison we also adopt the methods explained in Bîrzan et al. (2004) which consider the buoyancy time $t_{\rm buoy} \sim R/\sqrt{2gV/SC}$, where $g = GM_{<R}/R^2$ is the gravitational acceleration, V is the volume of the cavity, S is the cross section of the cavity, and $C = 0.75$ is the drag coefficient (Churazov et al. 2001), and the refill time $t_{\rm ref} \sim 2\sqrt{r/g}$, where r is the radius of the cavity. We calculate the gravitational acceleration at the distance of the cavities from the total mass profile derived by Morita et al. (2006), who estimate $M_{<R\sim 8.5\,{\rm kpc}} \sim 2 \times 10^{11} M_\odot$. We find that the age estimates agree to within a factor of 2, with the buoyancy times of $\sim 2.0 \times 10^7$ yr lying in between the sound crossing time of $\sim 1.8 \times 10^7$ yr and the refill times of $\sim 3.7 \times 10^7$ yr.

We estimate the gas luminosity inside the cooling radius ($r_{\rm cool} = 33$ kpc; Rafferty et al. 2006) as the bolometric X-ray luminosity, L_X, derived from a deprojection analysis of *XMM-Newton* spectra similar to that described in Section 4.2. We measure $L_X = 1.5 \times 10^{42}\,{\rm erg\,s^{-1}}$, which is consistent with the value of Rafferty et al. (2006). This indicates that the mechanical luminosity of the AGN outburst is large enough to balance the radiative losses. In fact, since the 235 MHz radio emission extends beyond the cavities, we may argue that there is more power in the jet and lobes than one can infer from the X-rays.

Table 3
Cavity Properties

Quantity	Cavity N		Cavity S	
	(Using V_X)	(Using $V_{\rm radio}$)	(Using V_X)	(Using $V_{\rm radio}$)
a (kpc)	5	10	4	10
b (kpc)	4.3	6	4	6
R (kpc)	8.4	15	8.6	15
V (cm^3)	1.14×10^{67}	4.43×10^{67}	7.88×10^{66}	4.43×10^{67}
p (erg cm^{-3})	2.5×10^{-11}	1.8×10^{-11}	3.2×10^{-11}	2.2×10^{-11}
pV (erg)	2.9×10^{56}	8.0×10^{56}	2.5×10^{56}	9.8×10^{56}
kT (keV)	0.75	0.84	0.83	0.95
$c_{\rm s}$ (km s^{-1})	440	465	463	495
$t_{\rm s}$ (yr)	1.9×10^7	3.2×10^7	1.8×10^7	3.0×10^7
$P_{\rm cav}$ (erg s^{-1})	2.0×10^{42}	3.2×10^{42}	1.8×10^{42}	4.2×10^{42}

Notes. Cavity volumes are calculated assuming spherical or prolate ellipsoidal shapes with semimajor axis a and semiminor axis b. In particular, X-ray volumes V_X are estimated from *Chandra* data and are consistent with the values of Bîrzan et al. (2004) and Rafferty et al. (2006), whereas radio volumes $V_{\rm radio}$ are estimated from GMRT observations at 235 MHz (see Section 3.2). Cavity powers $P_{\rm cav}$ are calculated assuming $4pV$ of energy per cavity and the sound crossing timescale $t_{\rm s}$. We adopt the temperature and density values estimated in the NE and SW sectors from *XMM-Newton* spectra (see the top left panel of Figure 5).

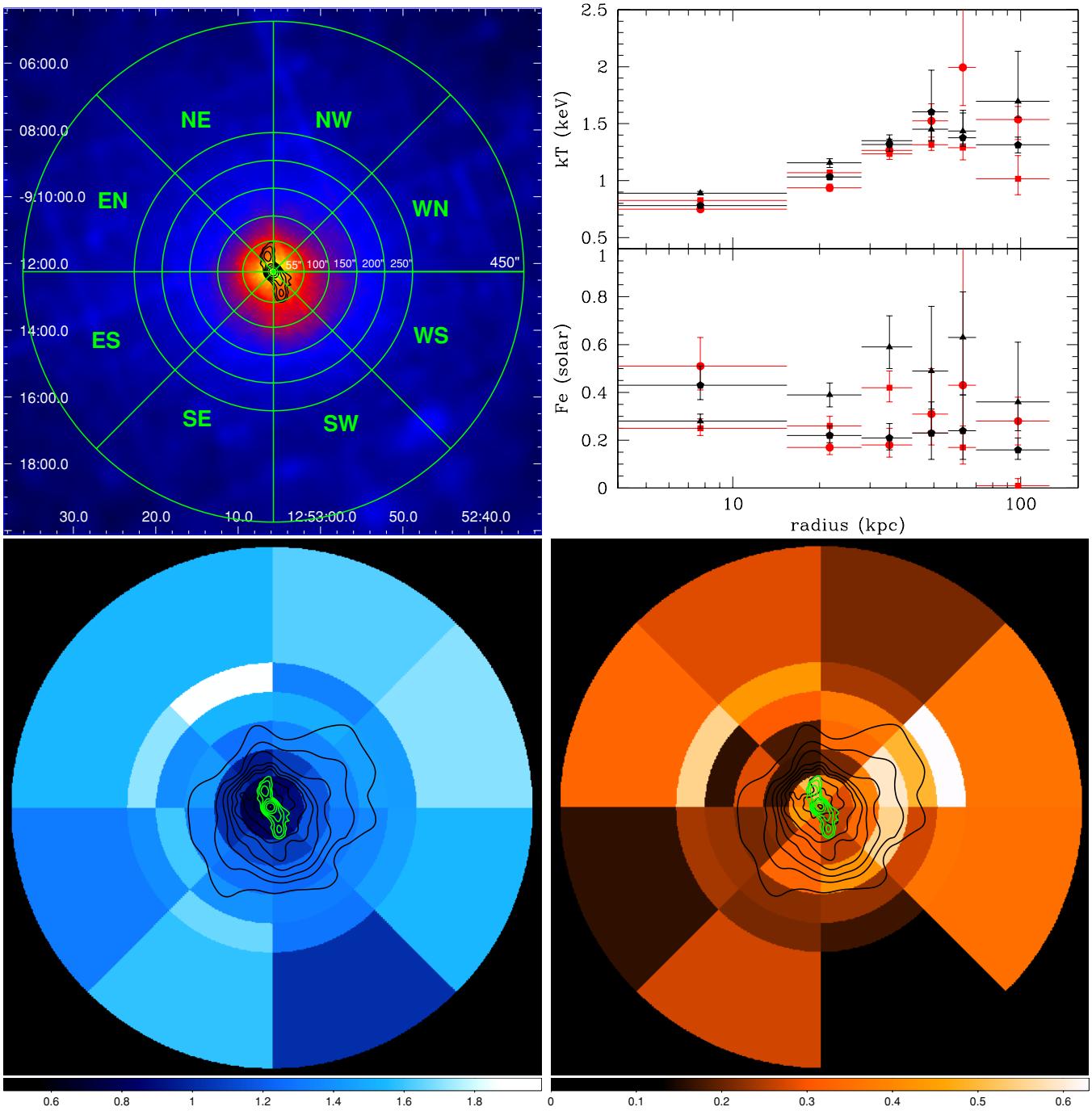

Figure 5. Top left: overlaid on the smoothed 0.5–2.0 keV *XMM-Newton* mosaic image are the sectors used for the spectral analysis (see Section 4.3 for details). 610 MHz GMRT radio contours are also shown to locate the position of the inner radio lobes. Top right: projected temperature (top panel) and Fe abundance (bottom panel) profiles measured with *XMM-Newton* along sector NE (red circles), sector SW (red squares), sector WN (black triangles), and sector ES (black pentagons). In red and black are indicated the profiles measured along and orthogonal to the cavities, respectively. Bottom: "wedge" temperature (left) and Fe abundance (right) maps derived from the *XMM-Newton* projected spectral fits in the sectoral annuli detailed in the top left figure. For comparison, *Chandra* contours and 610 MHz GMRT contours are overlaid in black and green, respectively.

(A color version of this figure is available in the online journal.)

The cavity volumes may be larger as the radio emission is less sensitive to projection effects than depressions in the X-ray image (as also pointed out by Bîrzan et al. 2008). By assuming that the cavities might be as extended as the radio lobes observed at 235 MHz, we estimate that cavity power could increase by a factor of ∼2 (see Table 3).

Recent studies have shown that the mechanical cavity power usually exceeds the radio luminosity of the bubbles in galaxy groups and clusters, with a large scatter from a few to a few thousands that seems to show a trend with the radio luminosity itself, i.e., the ratio of cavity power to radio luminosity increases with decreasing radio luminosities (Bîrzan et al. 2004, 2008). Thanks to the new GMRT radio data, we can compare the AGN mechanical power with the radio luminosity of the source in order to directly estimate its radiative efficiency. The monochromatic 235 MHz power of the total radio source is $P_{235} = 1.8 \times 10^{22}\,\mathrm{W\,Hz^{-1}}$. By assuming a spectral index $\alpha = 1.2$ (see Section 3.2), we measure the total radio luminosity over

the frequency range of 10 MHz–10 GHz to be 3.0×10^{38} erg s^{-1}, which is about 4 orders of magnitude less than the total power of the cavities. Therefore, the radio source in HCG 62 has a synchrotron radiative efficiency as low as $\sim10^{-4}$. This makes HCG 62 the least-efficient system in the Bîrzan et al. (2008) sample, and is a confirmation that the synchrotron radio luminosity is not a reliable gauge of the total mechanical power of the AGN outburst, as the radio sources can be very poor or time-variable radiators.

5.1.2. Pressure Balance

Since the radio source is filling the cavities, we can compare directly the radio pressure of the relativistic plasma internal to the lobes with the X-ray pressure of the surrounding thermal gas. The pressure of the hot gas is measured from the density and temperature derived from the X-ray data as $p = 2n_e kT$ (Section 4.2). In particular, for the X-ray pressure in the northern and southern cavities we assume the values estimated in the first bin by performing a deprojection analysis along the NE and SW sectors, respectively (see the top left panel of Figure 5). We find $p_{X,N} = 2.5\times10^{-11}$ erg cm^{-3} and $p_{X,S} = 3.2\times10^{-11}$ erg cm^{-3}. These values are consistent with the gas pressure at the radius of the cavities estimated by Morita et al. (2006).

The total pressure in a radio lobe is the sum of the magnetic pressure, p_B, and the total particle pressure, $p_{\rm part}$, and can be written as

$$p_{\rm radio} = p_B + p_{\rm part} = \frac{E_B}{\phi V} + \frac{1}{3}\frac{E_{\rm part}}{\phi V} = \frac{B^2}{8\pi} + \frac{1}{3}\frac{(1+k)E_e}{\phi V}, \quad (2)$$

where k is the ratio of the energy in protons to that in electrons (E_e), V is the volume of the radio lobe, and ϕ is the volume filling factor. Using the expression for E_e given in Pacholczyk (1970), Equation (2) determines the lobe pressure in terms of the magnetic field strength and the factor k/ϕ, once the volume V of the radio lobe is known. This calculation is usually performed under the widely adopted minimum energy conditions, in which the relativistic plasma is in equipartition with the magnetic field ($B_{\rm eq}$). For historical reasons the frequency band adopted to calculate the standard equipartition field is $\nu_1 = 10$ MHz to $\nu_2 = 100$ GHz, i.e., roughly the frequency range observable with radio telescopes. From a physical point of view, the adoption of this frequency band in the calculation of the minimum energy is equivalent to the assumption that only electrons emitting between 10 MHz and 100 GHz, i.e., with energy between $\gamma_{\rm min} \propto (\nu_1/B_{\rm eq})^{1/2}$ and $\gamma_{\rm max} \propto (\nu_2/B_{\rm eq})^{1/2}$, are present in the radio source. This approach neglects the contribution of the electrons emitting below 10 MHz and, as a more serious bias, in radio sources with different $B_{\rm eq}$ selects different energy bands of the electron population because the energy of the electrons which emit synchrotron radiation at a given frequency depends on the magnetic field intensity (Brunetti 2002). We therefore adopt a different approach to calculate the minimum energy conditions, in which $B_{\rm eq}$ does not depend on the emitted frequency band but directly on the low-energy cutoff of the electron spectrum. These so-called "revised" equipartition conditions select also the contribution to the energetics due to the low-energy electrons (Brunetti et al. 1997). In our calculations, we assume $\gamma_{\rm min} = 100$ and the observed spectral index (see Table 4).

The results of the equipartition calculations are reported in Table 4, where for comparison we also show the standard equipartition values. We estimate that the X-ray pressure is about 1 order of magnitude higher than the radio pressure, as typically found in cavity systems (e.g., Blanton et al. 2001; De Young 2006; Croston et al. 2008). We also find that with revised equipartition the cavities are closer to pressure balance than they are with standard equipartition. On the other hand, by assuming the lobes are in pressure equilibrium with the ambient gas we can obtain constraints on the particle content within the radio lobes (Dunn & Fabian 2004; Bîrzan et al. 2008). In particular, we determine the ratio $k_{\rm bal}$ of the energy in protons to that in electrons that is required to achieve pressure balance under revised equipartition conditions. We find $k_{\rm bal} \sim 300$–500, whereas higher values ($k_{\rm bal} \sim$ few thousands) are expected with standard equipartition. These values are in the range found by Bîrzan et al. (2008), who studied the energetics and particle content of the lobes of 24 radio galaxies in cooling cores, obtaining values of $k_{\rm bal}$ up to approximately 4000 (with standard equipartition). Based on an analysis of nine FR-I radio galaxies in a sample of groups of galaxies, Croston et al. (2008) found that the radio lobes are underpressured by a factor up to 70 (with revised equipartition, assuming $\gamma_{\rm min} = 10$ and $\alpha = 0.5$), and that the pressure imbalance appears to be linked to the radio-source morphology, i.e., "plumed" sources typically have larger pressure deficits than sources where the jets are embedded in the lobes ("bridged" sources). The authors interpret this result as evidence that plumed sources have a higher entrainment rate due to the larger fraction of the jet surface which is in direct contact with the external medium, leading to an increase in k/ϕ. Although the classification into bridged and plumed morphologies may not directly apply to radio sources at the center of cooling core systems, typically having amorphous structures, this picture is consistent with the results of Dunn et al. (2006) who argue that the large pressure imbalance observed in radio bubbles as those of the Perseus cluster is more likely to be due to entrainment rather than a relativistic proton population. Unfortunately, we cannot derive good constraints on the energy in relativistic particles without knowing the break frequency in the radio spectrum. However, we note that HCG 62 shows a disturbed radio morphology with inner lobes clearly filling the well-defined X-ray cavities, but with outer lobes having no associated X-ray cavities (see Section 3.2). Assuming their detection is not limited by the sensitivity of the current *Chandra* image, this suggests the possibility of mixing between ambient gas and radio plasma in the lobes. Therefore, the $k_{\rm bal} > 0$ values

Table 4
Results of Equipartition Calculations

Quantity	Cavity N		Cavity S	
	(revised)	(standard)	(revised)	(standard)
S_{235} (mJy)	6.0	6.0	5.4	5.4
S_{610} (mJy)	1.8	1.8	1.7	1.7
α_{235}^{610}	1.3	1.3	1.2	1.2
P_{235} (W Hz^{-1})	2.5×10^{21}	2.5×10^{21}	2.3×10^{21}	2.3×10^{21}
$\gamma_{\rm min}$	100	900	100	850
$B_{\rm eq}$ (μG)	6.7	3.1	6.6	3.3
$p_{\rm radio}$ (erg cm^{-3})	2.3×10^{-12}	4.8×10^{-13}	2.3×10^{-12}	5.5×10^{-13}
$p_X/p_{\rm radio}$	10.9	52.1	13.9	58.2
$k_{\rm bal}$	318	1830	500	2450

Notes. We assume $\phi = 1$, $k = 1$, and $V = V_X$ estimated in Section 5.1.1. A low-energy cutoff $\gamma_{\rm min} = 100$ of the electron spectrum is assumed to calculate the "revised" equipartition field, which implies a spectral frequency range of $\sim$280 kHz–100 GHz. We also show for comparison the results of the standard equipartition calculations, which adopt instead a fixed emitted frequency band of 10 MHz–100 GHz.

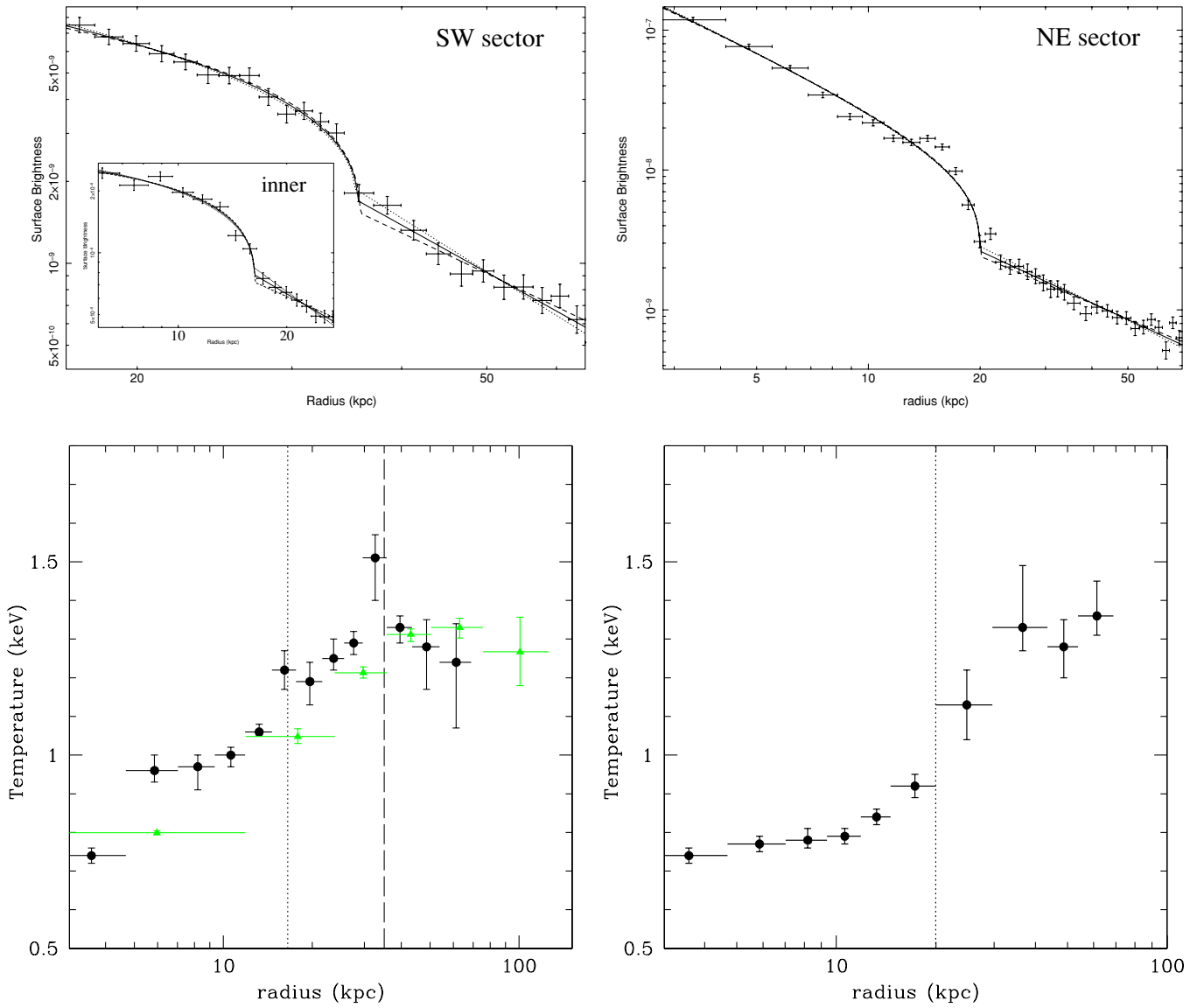

Figure 6. Top left: background-subtracted, exposure-corrected *Chandra* surface brightness profile extracted along the SW sector from P.A. 260° to 330° in the energy range 0.5–2.0 keV. The surface brightness is in counts cm^{-2} s^{-1}, with errors at 1σ. Radial error bars show the limits of the bins. The smooth curves show fits of the broken power-law density model which give density jumps of 1.47 (dotted), 1.65 (solid), and 1.86 (dashed), corresponding to Mach numbers of 1.32 (dotted), 1.45 (solid), and 1.62 (dashed). The radius of the shock is 36 kpc. The inner box shows the surface brightness profile of the inner front, which is at a radius of 16 kpc. The solid curve shows the fit of the broken power-law density model which gives a density jump of 1.77. Top right: similar to the top left panel, but for NE sector from P.A. 95° to 160°. The solid curve shows the fit of the broken power-law density model which gives a density jump of 2.27. The radius of the front is 20 kpc. Bottom left: *Chandra* (black circles) and *XMM-Newton* (green triangles) temperature profiles measured along the SW sector (the same sector as in the top left panel). The dashed line indicates the position of the shock ($r_{\rm shock} = 36$ kpc), while the dotted line indicates the position of the inner front ($r_{\rm front,SW} = 16$ kpc). Bottom right: *Chandra* temperature profile measured along the NE sector (the same sector as in the top right panel). The dotted line indicates the position of the front ($r_{\rm front,NE} = 20$ kpc). Error bars on temperature values are at 1σ.

(A color version of this figure is available in the online journal.)

that we measure in the lobes might be the results of entrainment of thermal gas through the group atmosphere.

5.2. Shock Fronts

We wish to investigate in more detail the morphological features presented in Section 3.1 by measuring the surface brightness and temperature profiles.

The surface brightness profile extracted along the SW sector within an aperture of 260°–330° (counting counterclockwise from P.A. = 0° toward the west) is shown in the top left panel of Figure 6. By fitting a broken power-law density model, at 36 kpc from the center we identify a clear break in surface brightness which corresponds to a jump in density of 1.65. To unambiguously determine the nature of this front, we extracted the temperature profile along the same sector (Figure 6, bottom left) and find that the region immediately interior to the front is significantly hotter than the undisturbed region just outside of it, with a temperature jump across the front of ∼14%. As discussed below, this is consistent with the interpretation of the front as a shock.

We also identify a front to the NE at 20 kpc from the center (see Figure 6, top right), that appears to have a symmetric feature to the SW (the surface brightness profile shows an edge at 16 kpc from the center, see the inner box in Figure 6, top left). We note that the detection of a temperature rise in the regions immediately inside of these fronts, which would be expected if they are shocks, is complicated by the underlying

rising temperature profile of the global group atmosphere (see Figure 6, bottom). For this reason, despite the lack of evidence for a temperature jump across the inner fronts, we cannot rule out the presence of shocks. In fact, the symmetric placement of these fronts and their proximity to the cavities (3–5 kpc outside the cavity edge) support their interpretation as weak shocks. Alternatively, they could be interpreted as cold fronts, caused by the subsonic expansion of the cavities displacing cool, low entropy gas outward. However, since we cannot place conclusive constraints on these features with the present data, we will not discuss them further in the paper and in the following we will focus only on the outer shock detected to the SW (simply referred to as "the shock").

A hydrodynamic model for the shock was made by initiating an explosion at the center of a hydrostatic, isothermal atmosphere with a power-law density profile. The power-law index for the density for the unshocked gas was determined from the broken power-law fit to the surface brightness profile. Our data are consistent with the presence of a shock having a Mach number $\mathcal{M} = 1.45$ and an age $\gtrsim 2.7 \times 10^7$ yr. Compared to a model with continuous energy injection, the point explosion produces a stronger, i.e., faster, shock at early times so its age estimate is a lower limit. For such a Mach number our model predicts the emission measure weighted temperature to rise by ∼15% across the front, which is in agreement with our measurements. As it appears evident from the comparison with the temperature profile obtained with *XMM-Newton* along the same sector (overlaid in green in Figure 6, bottom left), the detection of the temperature jump is possible only with the superb spatial resolution of *Chandra*. We estimate an energy $\sim 3.4 \times 10^{58}$ erg, and a power $\sim 4.0 \times 10^{43}$ erg s^{-1}, which is about 1 order of magnitude higher than the cavity power. The unusually large difference between the shock power and the cavity power is essentially due to the fact that the shock is much further away than the cavities from the group center ($R_{\rm shock} = 36$ kpc versus $R_{\rm cav} \sim 8.5$ kpc). Such a difference may be reduced by a factor of ∼2 if we adopt the cavity volume estimated from the radio data instead of that estimated from X-rays.

From a physical point of view, the difference in location and energetics between the shock and cavity system can be explained by two possibilities: (1) the shock and cavities are created by the same, violent AGN outburst and (2) the shock and cavities originate from different, multiple episodes of gentle AGN outbursts. (1) In the first case, the jet is initially supersonic and inflates the cavity violently, with much of the energy driving a shock. Once the jet slows the cavity rises buoyantly and the shock detaches from its tip and continues to propagate in the group atmosphere at a velocity $\mathcal{M}c_s$. By assuming that the shock was never any weaker than it is now and that the group atmosphere has an average temperature of ∼1 keV, we estimate the time for the shock to travel from the AGN to its current location to be $\lesssim 4.8 \times 10^7$ yr, which is consistent with the shock age estimated above. The shock age is also consistent with the refill timescale of the cavities, but slightly longer than the buoyancy timescale (see Section 5.1.1). The buoyancy timescale can be considered as an upper limit to the age of the outburst that produced the cavities, since it assumes the cavities were inflated at the group core and have risen slowly. If they formed close to their current location their age would be even shorter, and the conflict with the shock age more serious. (2) In the second case, it is possible that the shock originated during a previous AGN outburst which produced the outer radio lobes and perhaps an associated pair of cavities, though these are not detected in the existing data. In this scenario, the inner cavities are thought to be evacuated by the inner radio lobes during a more recent outburst, thus providing a natural explanation for the marginal difference between the buoyancy timescale of the cavities and the age of the shock. The expected older outer cavities might be detected with deeper exposures in a region close to the observed shock front.

However, with the current radio data we are not able to determine the relationship of the outer radio lobes to the inner ones. Therefore, considering also the uncertainties in the timescales estimated above, we cannot determine whether the observed radio/X-ray morphology is the result of one single AGN outburst, or multiple episodes. In either case, the position of the shock outside the S radio lobe makes plausible the interpretation of the shock as being directly driven by the lobe expansion triggered by an AGN outburst. Averaging over the past few 10^7 yr, the cavity power alone thus provides a lower limit to the true total mechanical power of the AGN. Inclusion of the energy in the shock provides a more complete estimate. The shock plus cavity power of $\sim 4.4 \times 10^{43}$ erg s^{-1} is much higher than the cooling luminosity ($L_X = 1.5 \times 10^{42}$ erg s^{-1}, estimated in Section 5.1.1). If the power level of 4.4×10^{43} erg s^{-1} is sustained, since it exceeds the power radiated by cooling core, either the core is currently being heated, or most of the power must be deposited in gas beyond the cooling core. The fact that the shock front is located at the outer edge of the cooling region is consistent with the latter.

On the other hand, the apparent absence of an outer shock front to the NE direction, which would be expected if the shock was created by the two outer radio lobes, requires some asymmetry. It is also possible that the shock strength varies with the position angle. In this case, the shock front may be in fact intrinsically symmetric and surrounding the whole central region of the group, but is detected only to the SW because of some difference in gas properties (e.g., higher density). We investigate further these possibilities also by means of a temperature map, which shows a lack of very cool (<0.9 keV) material on the SW side of the core (see Section 5.3.1) that might be explained by the shock.

5.3. Spectral Maps

Since no obvious feature associated with the cavities and radio lobes appear in the wedge maps (Section 4.3), we produced spectral maps with higher spatial resolution in order to investigate the two-dimensional temperature (Section 5.3.1) and iron abundance (Section 5.3.2) distribution independently of the choice of the sectors used to extract the spectra. Such spectral maps are suitable for identifying potentially interesting structures.

Chandra spectral maps were produced using a method similar to that described in O'Sullivan et al. (2005). The ACIS-S3 field of view was divided into a grid of square map pixels with side length 10 physical pixels (∼5″). For each of these map pixels a spectrum was extracted from a circular region centered on the pixel, with a radius chosen so as to obtain 800 net counts in the 0.3–5.0 keV band. Radii were allowed to vary between 10 and 100 physical pixels. Spectra and responses were created in an identical fashion to that used in our main spectral analysis and fitted with an absorbed `apec` model. Point sources were excluded from both spectra and the calculation of the spectral extraction region size and energies outside the 0.3–5.0 keV band were excluded. 90% uncertainties on parameters were estimated and any pixel with a temperature uncertainty greater than 15%

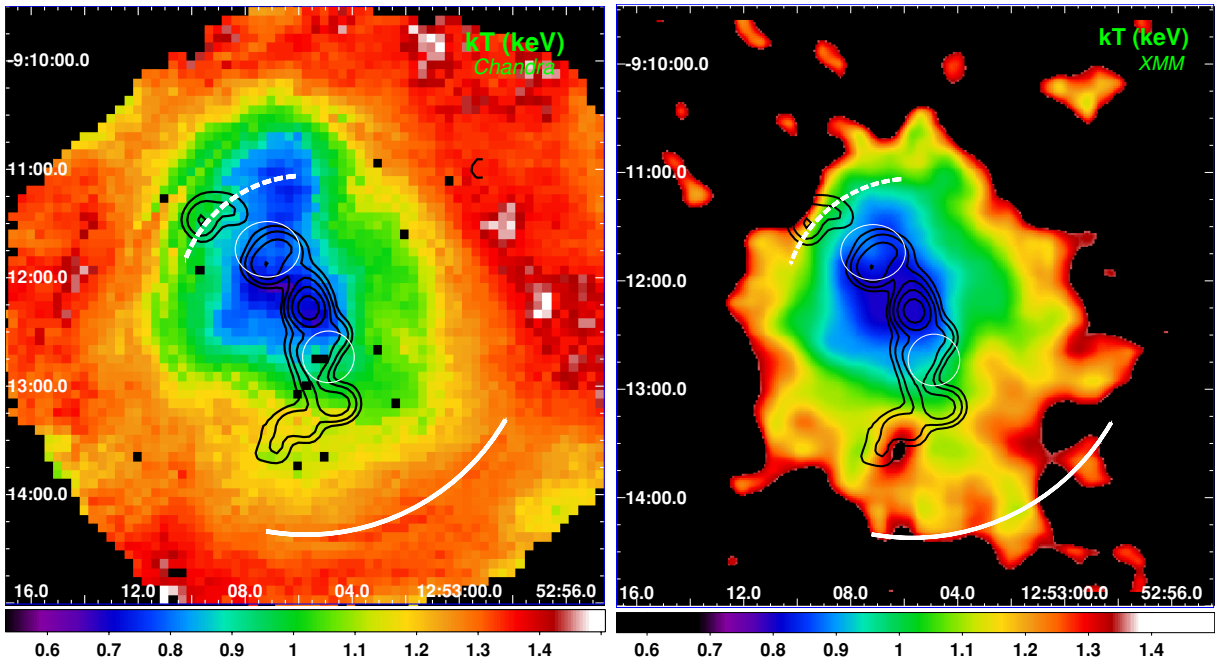

Figure 7. Left: *Chandra* temperature map with GMRT 235 MHz radio emission overlaid in black contours. Superposed in white are the two elliptical regions indicating the cavities (thin), and two arcs indicating the SW shock front (thick) and the NE front (thick dashed). Right: *XMM-Newton* temperature map obtained by means of the hardness ratio of different energy bands. Overlaid radio contours and superposed regions are the same as in left panel. Owing to the methods adopted to build such maps, the pixel values are not independent (see the text for details).

(A color version of this figure is available in the online journal.)

was excluded. The colors of the remaining map pixels indicate the best-fitting temperature, or abundance.

5.3.1. Temperature

In Figure 7 (left), we show the temperature map obtained from *Chandra* spectra. We also show in Figure 7 (right) a temperature image of the group central region built from *XMM-Newton* colors. Specifically, we extracted mosaicked MOS images in four different energy bands (0.5–1.0 keV, 1.0–2.0 keV, 2.0–4.5 keV, and 4.5–8.0 keV), subtract the background, and divide the resulting images by the exposure maps. A temperature in each square map pixel, chosen to have side length of 5 physical pixels (= 5.″5), is then obtained by fitting a thermal plasma model to the count rate estimated in the above energy bands in a surrounding area with a fixed radius of 15 physical pixels (= 16.″5).

The two temperature maps are consistent with each other and with previous results (Morita et al. 2006; Sanders et al. 2010), showing the presence of the cool core, but also the presence of cool gas in the region of the northern cavity. Owing to emission weighting in the large map extraction regions, this cold feature could be related to the presence of the cavity rims, which are indeed typically observed to be cold (McNamara & Nulsen 2007, and references therein). On the other hand, the lack of a comparable cold feature in the region of the southern cavity is notable. One possible explanation is that there was initially the presence of cold gas also to the south, but that this has then been heated by the passage of the shock. This argument could be taken as an indication of an asymmetric shock, or at least of an asymmetric shock strength, as discussed in Section 5.2.

5.3.2. Iron Abundance

In Figure 8, we show the iron abundance map obtained from *Chandra* spectra. The iron abundance distribution appears to be inhomogeneous, asymmetric, and lacking the usual central peak. We have reason to believe that the structures seen in the abundance map are real, as they are also observed in the maps of 90% upper and lower bound on abundance (not shown

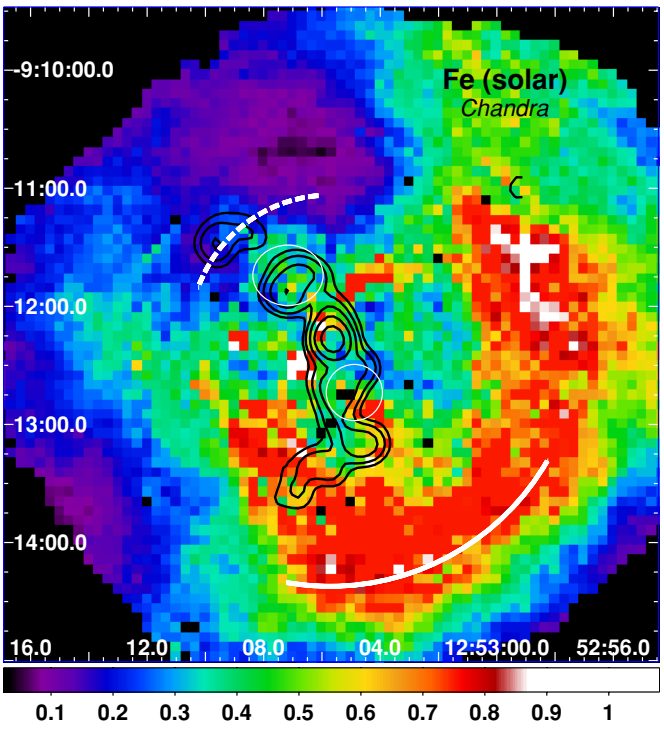

Figure 8. *Chandra* iron abundance map with GMRT 235 MHz radio emission overlaid in black contours. Superposed in white are the two elliptical regions indicating the cavities (thin), and the two arcs indicating the SW shock front (thick) and the NE front (thick dashed).

(A color version of this figure is available in the online journal.)

here). However, the uncertainties on the value of individual map pixels are large (30%–50%) and the variable sizing of spectral extraction regions produces an effect analogous to adaptive smoothing. It is therefore necessary to extract separate spectra to determine the true abundance of individual regions and the significance of any abundance differences. In particular, to confirm the presence of the arc-like region of enriched material visible at about 2′ to the SW of the group center, first discovered by Gu et al. (2007), we extract spectra from two elliptical regions centered at 2′ to the NE and SW of the group center along the direction of the inner radio lobes. The semimajor axis of both ellipses is orthogonal to the direction of the inner radio lobes and 1′ in extent, with the semiminor axis being half of it. We measure abundances of $0.12^{+0.06}_{-0.04}$ solar and $0.95^{+0.26}_{-0.16}$ solar (1σ errors) in the NE and SW regions, respectively. This indicates that the SW arc is more abundant than the NE dip at 5σ significance.

Gu et al. (2007) discuss several possibilities about the origin of the high-abundance gas, including entrainment during the cavity expansion triggered by the AGN activity, and ram pressure stripping due to tidal interaction of two central galaxies which have experienced a recent ($\sim 10^8$ yr) minor merger, as indicated by optical studies (Spavone et al. 2006). Unfortunately, we do not have enough information in the current data to disentangle this problem and the origin of the high-abundance arc-like region is still an open question. However, we stress here that the enriched material has a location and shape consistent with that of the newly discovered shock. Recent papers by Kaastra et al. (2009) and Prokhorov (2009) claim that in some cases, for instance near interfaces of hot and cold gas and near shocks, the usual approximation of Maxwellian electron distributions adopted for calculating thermal X-ray spectra is no longer valid. In such situations, the presence of non-thermal electrons modifies the line emissivities hence the X-ray spectrum, thus affecting the measurements of metal abundances. In particular, the best-fit iron abundance for the isothermal model is about 30% higher than the actual abundance (Kaastra et al. 2009). This could explain the high abundance arc that we measure. A similar effect of apparent iron overabundance may also be produced by the presence of non-equilibrium ionization states below the shock (Prokhorov 2010). These interpretations of the arc-like feature observed in the abundance map of HCG 62 are consistent with the presence of the detected shock front.

6. SUMMARY

We have analyzed new low-frequency GMRT radio data and existing *Chandra* and *XMM-Newton* X-ray data of the compact group HCG 62 in order to study the properties of the cavity system and the interplay with the central radio source. Our investigation demonstrates the power of a combined X-ray/radio approach to the feedback problem, and particularly the benefits of extending radio studies of AGNs to low frequencies where less energetic, older electron populations are visible. We summarize our main results below.

1. In contrast with the early classification of the HCG 62 cavity system as "radio ghost," the new GMRT observations detect low-frequency radio emission in the cavities.
2. The radio source has a total radio luminosity of 3.0×10^{38} erg s^{-1} and a very low radiative synchrotron efficiency of $\sim 10^{-4}$.
3. We estimate that the X-ray pressure of the cavities is about 1 order of magnitude higher than the "revised" equipartition pressure of the radio lobes. By assuming pressure balance, we find that the ratio of the energy in protons to that in electrons is ∼300–500, which may originate from thermal gas entrainment in the lobes through the group atmosphere.
4. We discover a Mach ∼1.5 shock front at 36 kpc from the center toward the SW, which has not been reported in the literature. The total energy in cavities and shock is $\sim 3.6 \times 10^{58}$ erg.
5. We confirm the presence of an arc-like region of enriched gas to the SW whose apparent high metallicity could be due to a non-Maxwellian electron distribution or non-equilibrium ionization states near the shock front.

We thank the anonymous referee for constructive suggestions that improved the presentation of the results. We thank S. Ettori for providing the software required to produce the *XMM-Newton* color map in Figure 7 (right) and M. Markevitch for useful discussions. M. Gitti also thanks T. Ponman and F. Brighenti for comments on the original manuscript. M. Gitti acknowledges support by grant ASI-INAF I/088/06/0. E. O'Sullivan acknowledges the support of the European Community under the Marie Curie Research Training Network. This research is supported by *Chandra* grant GO0-11003X.

REFERENCES

Anders, E., & Grevesse, N. 1989, Geochim. Cosmochim. Acta, 53, 197
Arnaud, M., Neumann, D. M., Aghanim, N., Gastaud, R., Majerowicz, S., & Hughes, J. P. 2001, A&A, 365, L80
Arnaud, M., et al. 2002, A&A, 390, 27
Bîrzan, L., McNamara, B. R., Nulsen, P. E. J., Carilli, C. L., & Wise, M. W. 2008, ApJ, 686, 859
Bîrzan, L., Rafferty, D. A., McNamara, B. R., Wise, M. W., & Nulsen, P. E. J. 2004, ApJ, 607, 800
Blanton, E. L., Randall, S. W., Douglass, E. M., Sarazin, C. L., Clarke, T. E., & McNamara, B. R. 2009, ApJ, 697, L95
Blanton, E. L., Sarazin, C. L., McNamara, B. R., & Wise, M. W. 2001, ApJ, 558, L15
Brunetti, G. 2002, in NATO Conf. Ser., The Role of VLBI in Astrophysics, Astronomy and Geodesy, ed. F. Mantovani & A. J. Kus (Dordrecht: Kluwer), 29
Brunetti, G., Setti, G., & Comastri, A. 1997, A&A, 325, 898
Buote, D. A. 2000, MNRAS, 311, 176
Carter, J., & Read, A. 2007, A&A, 464, 1155
Chandra, P., Ray, A., & Bhatnagar, S. 2004, ApJ, 612, 974
Churazov, E., Brüggen, M., Kaiser, C. R., Böhringer, H., & Forman, W. R. 2001, ApJ, 554, 261
Croston, J. H., Hardcastle, M. J., Birkinshaw, M., Worrall, D. M., & Laing, R. A. 2008, MNRAS, 386, 1709
David, L. P. 2009, Proc. 2009 Chandra Calibration Review, http://cxc.harvard.edu/ccr/proceedings/2009/presentations/david/
De Young, D. 2006, ApJ, 648, 200
Dickey, J. M., & Lockman, F. J. 1990, ARA&A, 28, 215
Diehl, S., Li, H., Fryer, C., & Rafferty, D. 2008, ApJ, 687, 173
Dunn, R. J. H., & Fabian, A. C. 2004, MNRAS, 355, 862
Dunn, R. J. H., & Fabian, A. C. 2006, MNRAS, 373, 959
Dunn, R. J. H., Fabian, A. C., & Celotti, A. 2006, MNRAS, 372, 1741
Dunn, R. J. H., Fabian, A. C., & Taylor, G. B. 2005, MNRAS, 364, 1343
Fabian, A. C., Sanders, J. S., Taylor, G. B., Allen, S. W., Crawford, C. S., Johnstone, R. M., & Iwasawa, K. 2006, MNRAS, 366, 417
Finoguenov, A., & Ponman, T. J. 1999, MNRAS, 305, 325
Finoguenov, A., Ponman, T. J., Osmond, J. P. F., & Zimer, M. 2007, MNRAS, 374, 737
Gastaldello, F., Buote, D., Brighenti, F., & Mathews, W. 2008, ApJ, 673, L17
Gastaldello, F., Buote, D., Humphrey, P., Zappacosta, L., Bullock, J., Brighenti, F., & Mathews, W. G. 2007, ApJ, 669, 158
Gastaldello, F., Buote, D., Temi, P., Brighenti, F., Mathews, W., & Ettori, S. 2009, ApJ, 693, 43
Giacintucci, S., Vrtilek, J. M., O'Sullivan, E., Raychaudhury, S., David, L. P., Venturi, T., Athreya, R., & Gitti, M. 2009, in AIP Conf. Proc. Ser. 1201, The Monster's Fiery Breath: Feedback in Galaxies, Groups, and Clusters, ed. S. Heinz & E. Wilcots (Melville, NY: AIP), 229
Giacintucci, S., et al. 2007, A&A, 476, 99

Giacintucci, S., et al. 2008, ApJ, 682, 186
Gitti, M., McNamara, B. R., Nulsen, P. E. J., & Wise, M. W. 2007, ApJ, 660, 1118
Gu, J., Xu, H., Gu, L., An, T., Wang, Y., Zhang, Z., & Wu, X.-P. 2007, ApJ, 659, 275
Johnson, R., Ponman, T. J., & Finoguenov, A. 2009, MNRAS, 395, 1287
Kaastra, J. S., Bykov, A. M., & Werner, N. 2009, A&A, 503, 373
Kaastra, J. S., et al. 2004, A&A, 413, 415
McNamara, B. R., & Nulsen, P. E. J. 2007, ARA&A, 45, 117
Morita, U., Ishisaki, Y., Yamasaki, N. Y., Ota, N., Kawano, N., Fukazawa, Y., & Ohashi, T. 2006, PASJ, 58, 719
O'Sullivan, E., Vrtilek, J. M., Kempner, J. C., David, L. P., & Houck, J. C. 2005, MNRAS, 357, 1134
O'Sullivan, E., et al. 2010, MNRAS, submitted
Pacholczyk, A. G. 1970, Radio Astrophysics: Nonthermal Processes in Galactic and Extragalactic Sources, Series of Books in Astronomy and Astrophysics (San Francisco, CA: Freeman)
Peterson, J. R., & Fabian, A. C. 2006, Phys. Rep., 427, 1
Peterson, J. R., Kahn, S. M., Paerels, F. B. S., Kaastra, J. S., Tamura, T., Bleeker, J. A. M., Ferrigno, C., & Jernigan, J. G. 2003, ApJ, 590, 207
Petrosian, V., & Dickey, J. 1973, ApJ, 186, 403
Ponman, T. J., & Bertram, D. 1993, Nature, 363, 51
Prokhorov, D. A. 2009, A&A, 508, 69
Prokhorov, D. A. 2010, A&A, 509, 29
Rafferty, D., McNamara, B. R., Nulsen, P. E. J., & Wise, M. W. 2006, ApJ, 652, 216
Rasmussen, J., & Ponman, T. 2007, MNRAS, 380, 1554
Raychaudhury, S., Giacintucci, S., O'Sullivan, E., Vrtilek, J., Croston, J., Athreya, R., David, L., & Venturi, T. 2009, in ASP Conf. Ser. 407, The Low-Frequency Radio Universe, ed. D. J. Saikia, D. A. Green, Y. Gupta, & T. Venturi (San Francisco, CA: ASP), 246
Sanders, J. S., Fabian, A. C., Allen, S. W., Morris, R. G., Graham, J., & Johnstone, R. M. 2008, MNRAS, 385, 1186
Sanders, J. S., Fabian, A. C., Frank, K. A., Peterson, J. R., & Russell, H. R. 2010, MNRAS, 402, 127
Spavone, M., Iodice, E., Longo, G., Paolillo, M., & Sodani, S. 2006, A&A, 457, 493
Sun, M. 2009, ApJ, 704, 1586
Sun, M., Voit, G. M., Donahue, M., Jones, C., Forman, W., & Vikhlinin, A. 2009, ApJ, 693, 1142
Tokoi, K., et al. 2008, PASJ, 60S, 317
Valluri, M., & Anupama, G. C. 1996, AJ, 112, 1390
Vrtilek, J. M., Grego, L., David, L. P., Ponman, T. J., Forman, W., Jones, C., & Harris, D. E. 2002, Am. Phys. Soc. Meeting, B17.107